

# Microfield distributions in strongly coupled two-component plasmas

H. B. Nersisyan,\* C. Toepffer, and G. Zwicknagel

*Institut für Theoretische Physik II, Erlangen-Nürnberg Universität,  
Staudtstrasse 7, D-91058 Erlangen, Germany*

(Dated: November 11, 2018)

The electric microfield distribution at charged particles is studied for two-component electron-ion plasmas using molecular dynamics simulation and theoretical models. The particles are treated within classical statistical mechanics using an electron-ion Coulomb potential regularized at distances less than the de Broglie length to take into account the quantum-diffraction effects. The potential-of-mean-force (PMF) approximation is deduced from a canonical ensemble formulation. The resulting probability density of the electric microfield satisfies exactly the second-moment sum rule without the use of adjustable parameters. The correlation functions between the charged radiator and the plasma ions and electrons are calculated using molecular dynamics simulations and the hypernetted-chain approximation for a two-component plasma. It is shown that the agreement between the theoretical models for the microfield distributions and the simulations is quite good in general.

PACS numbers: 52.27.Gr, 52.27.Aj, 52.65.Yy, 05.10.-a

## I. INTRODUCTION

Because of the Stark effect, the fluctuating electric microfields created by the charged particles in a plasma influence its optical and thermodynamic properties. They affect the profiles of spectral lines (broadening and shift) and effectively lower the photoionization thresholds of atoms and ions immersed in a plasma [1, 2, 3]. A comparison of experimental and theoretical widths and shapes of the Stark-broadened spectral lines is widely used for plasma diagnostics [4, 5].

Under certain assumptions [1, 2], the observed spectral line shapes can be closely related to the electric microfield distribution at the radiating atom or ion (radiator) [6, 7]. Within the quasistatic approximation the problem is then reduced to a determination of the probability distribution of the low-frequency component of the perturbing electric fields. This is mainly associated with the distribution of the heavier perturbing particles, i.e. the ions, whereas the electrons can be assumed

---

\*Permanent address: Institute of Radiophysics and Electronics, 378410 Ashtarak, Armenia; Electronic address: nersisyan@theorie2.physik.uni-erlangen.de

to adjust instantaneously to the configuration of the ions.

Since the pioneering work of Holtsmark [6], who completely neglected correlations between the particles (ideal plasma), many efforts have been concentrated on an improved statistical description of the microfield distribution. The first theory which goes beyond the Holtsmark limit and which is based on a cluster expansion similar to that of Ursell and Mayer [8] was developed by Baranger and Mozer [9, 10]. In this approach the microfield distribution is represented as an expansion in terms of correlation functions which has been truncated on the level of the pair correlation. The latter is treated in the Debye-Hückel form which corresponds to the first order of the expansion in the coupling parameter. The theory by Baranger and Mozer was improved by Hooper [11, 12] and later by Tighe and Hooper [13, 14]. Based on Broyles' collective-coordinate technique [15] they reformulated the expansion of the microfield distribution in terms of other functions by introducing a free parameter which was adjusted in such a way to arrive at a level where the resulting microfield distribution did not depend on the free parameter any more. A further improvement of this model was made in Ref. [16] considering a Debye-chain cluster expansion. Afterwards the Baranger-Mozer second order theory was extended by including higher order corrections, like the triple correlation contribution [17, 18]. However, it was argued that such a method is only valid for low-density, high-temperature plasmas, i.e. at small coupling parameters, where the correction to the Holtsmark distribution, corresponding to the first term in the series, is small. In the limit of very strong coupling and without screening Meyer's harmonic oscillator model is applicable [19], in which every ion is assumed to oscillate independently of the others around its equilibrium position at the ion-sphere center. The first theory capable to provide reliable numerical results for strongly coupled plasmas, known as adjustable-parameter exponential approximation (APEX), was proposed by Iglesias, Lebowitz *et al.* [20, 21, 22, 23, 24]. This phenomenological but highly successful approximation is based on a special parameterization of the electric microfield produced on a radiator. It involves a non-interacting quasiparticle representation of the electron-screened ions, designed to yield the correct second moment of the microfield distribution. APEX was first developed for three- and two-dimensional Coulomb systems [21, 22] and later adapted to screened Coulomb systems and ion mixtures [23, 24]. (See also Ref. [25] for the corrected version of APEX for a neutral radiator). Another approach providing reliable numerical results for the strongly coupled plasmas was proposed by Iglesias [26]. Following the idea of Morita [27] on the similarity of the representation of the microfield distribution to that of the excess chemical potential, Iglesias reduced the problem to a determination of the radial distribution function (RDF) for a fictitious system with an imaginary part in the interaction energy. Employing this idea Lado and Dufty

[28, 29, 30] developed an integral equation technique for calculating the RDF and good agreement was found with computer simulations. It is now possible to calculate the microfield distribution from Monte Carlo (MC) or molecular-dynamics (MD) simulations of plasmas [31, 32, 33, 34, 35]. These methods allows to study the effects of microfield nonuniformity [36, 37] and the dynamical properties of the electric microfield [35, 38] as well as to simulate the high-frequency microfield distribution in electron plasmas [35, 39]. With these powerful tools one can check the accuracy of theoretical models and establish asymptotic or analytic fitting formulas suitable for applications (see, e.g. [40, 41] and references therein).

Until now most work was done on either electronic or ionic one-component plasmas (OCP) neglecting the influence of the attractive interactions between electrons and ions. Here we treat ions and electrons on an equal footing by concentrating on two-component plasmas (TCP). Previously this has been done in Ref. [42] for partially degenerate electrons. In particular, the low-frequency component of the microfield was calculated within the linear response treatment taking strong correlations into account via local field corrections. Also the problem of attractive interaction has been considered for single but highly charged impurity ion immersed in an electronic OCP (see, e.g. Ref. [43] for a recent review of these cases).

In the present paper we study strongly coupled systems, i.e. a highly charged radiator in a TCP of classical (nondegenerated) and strongly correlated particles beyond a perturbative treatment. As in Ref. [42] the presented theoretical scheme is based on the potential-of-mean-force (PMF) approximation which exactly satisfies the sum-rule requirement arising from the second moment of the microfield distribution without introducing adjustable parameters. Another important ingredient is the electron-ion attractive interaction which drastically changes the physical properties of the system as compared to classical OCPs (see, e.g., [43]). This may cause significant changes in the microfield distribution on either neutral or charged radiators. But the thermodynamic stability of a TCP requires some quantum features for the electron-ion interaction at short distances. Here we focus on an application of classical statistical mechanics and MD simulations which is enabled by using a regularized ion-electron potential where the divergence at the origin is removed [27, 44], see also [43, 45] for a review.

The paper is organized as follows. In Sec. II, we define the systems and parameters of interest as well as the theoretical model to calculate the microfield distribution in a TCP. The exact second moment for the charged radiator is calculated in Sec. III. The theoretical schemes applied previously to either electronic or ionic OCPs are generalized to TCPs in Sec. IV. In particular, we consider the Holtsmark distribution, express the microfield distribution through the pair dis-

tribution functions, and deduce the PMF approximation from the classical canonical ensemble. Furthermore we construct a theoretical approach based on the exponential approximation where the effective electric fields are calculated on the basis of the PMF approximation and the pair correlation functions. In Sec. V we consider the hypernetted-chain (HNC) integral equations technique to calculate these functions in a two component plasma. In order to test the theoretical models we carried out classical MD simulations to calculate both the pair correlation functions and the microfield distribution. Technical aspects and the numerical results are presented in Sec. V. These results are summarized in Sec. VI. Some details of the calculations are described in the Appendix.

## II. MICROFIELD DISTRIBUTION IN A TCP: THEORETICAL BACKGROUND

### A. Basic parameters for the TCP

We consider a neutral and isotropic two component electron-ion plasma consisting of  $N_i$  ions and  $N_e$  electrons at a temperature  $T$  in a volume  $\Omega$ . The particles are assumed to be classical and pointlike. The average densities, charges and masses of the ions and electrons are  $n_i = N_i/\Omega$ ,  $n_e = N_e/\Omega$ , and  $Ze$ ,  $-e$  and  $m_i$ ,  $m$ , respectively. We assume that the density of radiator ions are small,  $n_R \ll n_{i;e}$  and thus consider only one radiator ion with charge  $Z_R e$  in our calculations (throughout this paper the index  $R$  refers to the radiators). Because of the charge neutrality we have  $N_i Z - N_e + Z_R = 0$ . In the thermodynamic limit ( $N_{i;e} \rightarrow \infty$  and  $\Omega \rightarrow \infty$ ) this is equivalent to  $n_e = n_i Z$ .

We now introduce the Coulomb coupling parameters  $\Gamma_{\alpha\beta}$  which play an important role for characterizing the properties of a TCP. Introducing the Wigner-Seitz radii, i.e. the mean electron-electron, electron-ion and ion-ion distances through the relations,  $a_e^{-3} = 4\pi n_e/3$ ,  $a^{-3} = 4\pi n/3$  and  $a_i^{-3} = 4\pi n_i/3$  (where  $n = n_e + n_i$  is the plasma total density) these parameters are defined as

$$\Gamma_{ee} = \frac{e_S^2}{a_e k_B T}, \quad \Gamma_{ei} = \frac{Ze_S^2}{a k_B T}, \quad \Gamma_{ii} = \frac{Z^2 e_S^2}{a_i k_B T}, \quad (1)$$

respectively, where  $e_S^2 = e^2/4\pi\epsilon_0$ . Note that

$$\Gamma_{ee} = \frac{\Gamma_{ei}}{[Z^2(Z+1)]^{1/3}}, \quad \Gamma_{ii} = \frac{Z\Gamma_{ei}}{(Z+1)^{1/3}}. \quad (2)$$

In a hydrogen plasma with  $Z = 1$  we obtain  $\Gamma_{ee} = \Gamma_{ii} = 2^{-1/3}\Gamma_{ei}$  while in a plasma with highly charged ions ( $Z \gg 1$ )  $\Gamma_{ii} = Z^{2/3}\Gamma_{ei}$  and  $\Gamma_{ee} = \Gamma_{ei}/Z$ . For  $Z \geq 2$  the coupling parameters satisfy the inequality  $\Gamma_{ee} < \Gamma_{ei} < \Gamma_{ii}$ .

Here we consider the pair interaction potential  $e_S^2 q_\alpha q_\beta u_{\alpha\beta}(r)$  with  $\alpha; \beta = e, i, R$ ,  $q_e = -1$ ,  $q_i = Z$ ,  $q_R = Z_R$ , and

$$u_{\alpha\beta}(r) = \frac{1}{r} \left( 1 - e^{-r/\delta_{\alpha\beta}} \right) \quad (3)$$

which is regularized at small distances due to quantum-diffraction effects. In this paper we assume that the Coulomb potential is cutoff at the thermal de Broglie wavelengths,  $\delta_{\alpha\beta} = (\hbar^2/\mu_{\alpha\beta}k_B T)^{1/2}$ , where  $\mu_{\alpha\beta}$  is the reduced mass of the particles  $\alpha$  and  $\beta$ . For large distances  $r > \delta_{\alpha\beta}$  the potential becomes Coulomb, while for  $r < \delta_{\alpha\beta}$  the Coulomb singularity is removed and  $u_{\alpha\beta}(0) = 1/\delta_{\alpha\beta}$ . By this the short range effects based on the uncertainty principle are included [27, 43, 44, 45].

For a classical description of a plasma the electron degeneracy parameter  $\Theta_e$ , i.e. the ratio of the thermal energy and the Fermi energy must fulfill  $\Theta_e = k_B T/E_F > 1$ . Or, alternatively, the electron thermal wavelength should be smaller than the electron-electron mean distance,  $\delta_{ee} < 2(4/9\pi)^{1/3} a_e \simeq 1.04 a_e$ . Since an ion is much heavier than an electron this condition is usually fulfilled for ions. We note that  $\delta_{ii} \ll \delta_{ei}$  and  $\delta_{ee} \simeq 2^{1/2} \delta_{ei}$  since  $\mu_{ei} \simeq m$ . Therefore one can expect that the regularization given by Eq. (3) is less important for ions than for electrons. Furthermore, scattering of any two particles is classical for impact parameters that are large compared to the de Broglie wavelengths. Typical impact parameters are given by the Landau lengths,  $\lambda_{L\alpha\beta} = e_S^2 |q_\alpha q_\beta| / k_B T$ . Its ratio to the de Broglie wavelengths is given by

$$\sigma_{\alpha\beta} = \frac{\lambda_{L\alpha\beta}}{\delta_{\alpha\beta}} = \Gamma_{ei} \frac{|q_\alpha q_\beta|}{Z} \frac{a}{\delta_{\alpha\beta}} = \frac{e_S^2 |q_\alpha q_\beta| u_{\alpha\beta}(0)}{k_B T}. \quad (4)$$

This is also the maximum value of the interparticle interaction energy in the units of  $k_B T$ , where  $\sigma_{ee} < \sigma_{ei} \ll \sigma_{ii}$  and  $\sigma_{ei} \simeq 2^{1/2} Z \sigma_{ee}$ . Classical description of the scattering events in the TCP is valid if  $\sigma_{ee} > 1$ . This can be alternatively written in the explicit form  $k_B T < 1 \text{ Ry}$ . Combining this condition with the one considered above we finally obtain the temperature domain where the classical treatment is adequate,  $E_F < k_B T < 1 \text{ Ry}$ . This condition occurs at lower densities of electrons. Since the parameter  $\delta_{ee}$  increases with electron-ion Coulomb coupling the classical condition  $\sigma_{ee} > 1$  implies that the state with stronger  $\Gamma_{ei}$  behaves more classical as discussed in Ref. [43].

## B. Microfield distribution formulation within thermodynamic canonical ensemble

The electric microfield distribution (MFD)  $Q(\boldsymbol{\varepsilon})$  is defined as the probability density of finding a field  $\mathbf{E} = \boldsymbol{\varepsilon}$  at a charge  $Z_R e$ , located at  $\mathbf{r}_0$ , in a TCP with  $N_i$  ions and  $N_e$  electrons. This system

is described by classical statistical mechanics in a canonical ensemble of  $(N_i + N_e + 1)$  particles, and temperature  $T$ . The normalized probability density of the microfield  $\boldsymbol{\varepsilon}$  in the thermodynamic limit is then given by

$$Q(\boldsymbol{\varepsilon}) = \frac{1}{W} \int_{\Omega} e^{-\beta_T U(\mathcal{T}_e, \mathcal{T}_i, \mathbf{r}_0)} \delta(\boldsymbol{\varepsilon} - \mathbf{E}(\mathcal{T}_e, \mathcal{T}_i, \mathbf{r}_0)) d\mathbf{r}_0 d\mathcal{T}_e d\mathcal{T}_i, \quad (5)$$

where  $\beta_T = 1/k_B T$ , and  $\mathcal{T}_e = \{\mathbf{r}_1, \mathbf{r}_2 \dots \mathbf{r}_{N_e}\}$ ,  $\mathcal{T}_i = \{\mathbf{R}_1, \mathbf{R}_2 \dots \mathbf{R}_{N_i}\}$  are the coordinates of electrons and ions, respectively. Here

$$W = \int_{\Omega} e^{-\beta_T U(\mathcal{T}_e, \mathcal{T}_i, \mathbf{r}_0)} d\mathbf{r}_0 d\mathcal{T}_e d\mathcal{T}_i \quad (6)$$

is the canonical partition function and  $U(\mathcal{T}_e, \mathcal{T}_i, \mathbf{r}_0)$  is the potential energy of the configuration

$$U(\mathcal{T}_e, \mathcal{T}_i, \mathbf{r}_0) = U_{ee}(\mathcal{T}_e) + U_{ii}(\mathcal{T}_i) + U_{ei}(\mathcal{T}_e, \mathcal{T}_i) + U_{eR}(\mathcal{T}_e, \mathbf{r}_0) + U_{iR}(\mathcal{T}_i, \mathbf{r}_0) \quad (7)$$

with electron-electron, ion-ion, electron-ion, electron-radiator and ion-radiator interaction terms, respectively. Assuming spherical symmetric interactions between the particles the interaction terms in Eq. (7) can be represented as

$$U_{\alpha\beta}(\mathcal{T}_\alpha, \mathcal{T}_\beta) = \vartheta_{\alpha\beta} q_\alpha q_\beta e_S^2 \sum_{a,b} u_{\alpha\beta} \left( \left| \mathbf{r}_a^{(\alpha)} - \mathbf{r}_b^{(\beta)} \right| \right), \quad (8)$$

$$U_{\alpha R}(\mathcal{T}_\alpha, \mathbf{r}_0) = q_\alpha Z_R e_S^2 \sum_a u_{\alpha R} \left( \left| \mathbf{r}_0 - \mathbf{r}_a^{(\alpha)} \right| \right) \quad (9)$$

in terms of the pair interaction potentials  $u_{\alpha\beta}(r)$  and  $u_{\alpha R}(r)$ , where  $\alpha; \beta = e; i$ ,  $\vartheta_{ee} = \vartheta_{ii} = 1/2$ ,  $\vartheta_{ei} = 1$ ,  $\mathbf{r}_a^{(e)} = \mathbf{r}_a$ ,  $\mathbf{r}_a^{(i)} = \mathbf{R}_a$ . In Eq. (8) the sum is restricted to  $a \neq b$  for like particles,  $\alpha = \beta$ . The total electrical field  $\mathbf{E}(\mathcal{T}_e, \mathcal{T}_i, \mathbf{r}_0)$  acting on the radiator is given by the superposition of electronic and ionic single-particle fields

$$\mathbf{E}(\mathcal{T}_e, \mathcal{T}_i, \mathbf{r}_0) = -\frac{1}{Z_R e} \nabla_0 U = \mathbf{E}_e(\mathcal{T}_e, \mathbf{r}_0) + \mathbf{E}_i(\mathcal{T}_i, \mathbf{r}_0) \quad (10)$$

with

$$\mathbf{E}_\alpha(\mathcal{T}_\alpha, \mathbf{r}_0) = \sum_{a=1}^{N_\alpha} \mathbf{E}_\alpha \left( \mathbf{r}_0 - \mathbf{r}_a^{(\alpha)} \right). \quad (11)$$

As  $\mathbf{E}_e(\mathbf{r}) = \frac{e}{r} \mathbf{E}_e(r)$ ,  $\mathbf{E}_i(\mathbf{r}) = \frac{e}{r} \mathbf{E}_i(r)$ , we obtain for the electronic and ionic single-particle fields  $E_e(r) = e_F u'_{eR}(r)$ ,  $E_i(r) = -Z e_F u'_{iR}(r)$ , where the prime indicates derivative with respect to  $r$ , and  $e_F = e/4\pi\epsilon_0$ .

The spherical symmetric interaction between plasma particles allows to introduce the normalized microfield distribution  $P(\varepsilon) = 4\pi\varepsilon^2 Q(\varepsilon)$ . It is useful to consider the Fourier transform of  $Q(\varepsilon)$  defined by

$$T(\mathbf{K}) = \int Q(\varepsilon) e^{i\mathbf{K}\cdot\mathbf{\varepsilon}} d\varepsilon = \langle e^{i\mathbf{K}\cdot\mathbf{E}} \rangle. \quad (12)$$

Here  $\langle \dots \rangle$  denotes a statistical average. Again we note that due to the isotropy of the system the Fourier transform of the MFD must behave as

$$T(K) = \int_0^\infty P(\varepsilon) j_0(K\varepsilon) d\varepsilon, \quad P(\varepsilon) = \frac{2\varepsilon^2}{\pi} \int_0^\infty T(K) j_0(K\varepsilon) K^2 dK, \quad (13)$$

where  $j_0(x) = \sin x/x$  is the spherical Bessel function of order zero. The coefficients of the expansion of the function  $T(K)$  at  $K \rightarrow 0$  yield the even moments of the microfield distribution,

$$T(K) = 1 - \frac{K^2}{6} \langle E^2 \rangle + \frac{K^4}{120} \langle E^4 \rangle - \dots \quad (14)$$

The similar expansion for the function  $\mathcal{L}(K)$  defined by  $T(K) = e^{-\mathcal{L}(K)}$  yields

$$\mathcal{L}(K) = \frac{K^2}{6} \langle E^2 \rangle + \frac{K^4}{72} \left[ \langle E^2 \rangle^2 - \frac{3}{5} \langle E^4 \rangle \right] + \dots \quad (15)$$

Therefore the Fourier transform of the MFD can be interpreted as a generating function for microfield even moments. Moreover, Eqs. (14) and (15) suggest a simple criterion for the existence of even moments. In particular, the second moment of the MFD exists if the function  $\mathcal{L}(K)$  and its first and second derivatives are regular at the origin. Eqs. (5)-(15) then describe the total MFD at the position  $\mathbf{r}_0$  of the radiator generated by both the statistically distributed ions and electrons of the TCP. Since we are interested to calculate the MFD, Eq. (5), in an infinite system the statistical average of any quantity becomes translationally invariant with respect to  $\mathbf{r}_0$ , and the location of the test charge may be taken as the origin without loss of generality.

### III. SECOND MOMENT

A knowledge of moment sum rules is often useful in developing approximation schemes for fluids and plasmas. The moments of the MFD fix the shape of the distribution and involves some useful information about the system. For example, the exact second moment has been previously incorporated into the calculation of the MFDs in the APEX scheme. Here, we derive exact expressions for the second moment of the MFD on charged radiators. Note that in general the existence of the second moment requires that the MFD decays at large electric fields faster than  $\varepsilon^{-3}$ .

Let us consider the exact expression for the second moment of the microfield distribution in the TCP and for a charged radiator. The second moment may be written in the form

$$\langle E^2 \rangle = \frac{1}{(Z_R e)^2} \langle (\nabla_0 U)^2 \rangle, \quad (16)$$

where  $\nabla_0$  is the gradient with respect to  $\mathbf{r}_0$  and the average is over the canonical ensemble defined in Eq. (5). Noting that  $e^{-\beta_T U} (\nabla_0 U) = -k_B T (\nabla_0 e^{-\beta_T U})$ , substituting this relation into Eq. (16), integrating by parts, and setting the surface terms equal to zero yields

$$\langle E^2 \rangle = \frac{k_B T}{(Z_R e)^2} \langle \nabla_0^2 U \rangle = -\frac{k_B T}{Z_R e} \langle (\nabla_0 \cdot \mathbf{E}) \rangle. \quad (17)$$

We now use Eqs. (10) and (11), the relation  $\nabla \cdot \mathbf{E}_\alpha(\mathbf{r}) = (q_\alpha e_F / r^2) \tilde{u}_\alpha(r)$ , where  $\tilde{u}_\alpha(r) = -[r^2 u'_{\alpha R}(r)]'$ , and translational symmetry. This yields

$$\langle E^2 \rangle = \frac{k_B T n_e}{Z_R \varepsilon_0} \left[ \int_0^\infty \tilde{u}_e(r) g_{eR}(r) dr - \int_0^\infty \tilde{u}_i(r) g_{iR}(r) dr \right]. \quad (18)$$

The functions  $g_{\alpha R}(r)$  are the pair correlation functions between radiator and the plasma particles, where  $n_\alpha g_{\alpha R}(r)$  is the density of plasma particles  $\alpha$  at a distance  $r$  from the radiator. These functions can be represented as

$$g_{eR}(r_1) = \frac{\Omega^2}{W} \int_{\Omega} e^{-\beta_T U(\mathcal{T}_e, \mathcal{T}_i)} d\mathcal{T}_e^{(1)} d\mathcal{T}_i, \quad (19)$$

$$g_{iR}(R_1) = \frac{\Omega^2}{W} \int_{\Omega} e^{-\beta_T U(\mathcal{T}_e, \mathcal{T}_i)} d\mathcal{T}_e d\mathcal{T}_i^{(1)}. \quad (20)$$

Here  $d\mathcal{T}_\alpha^{(s)} = \prod_{a=s+1}^{N_\alpha} d\mathbf{r}_a^{(\alpha)}$  is the reduced volume element in a phase space which does not involve the particles  $1, 2, \dots, s$  of plasma species  $\alpha$ . The interaction potential energy,  $U(\mathcal{T}_e, \mathcal{T}_i)$ , does not depend on  $\mathbf{r}_0$ . The pair correlation functions given by Eqs. (19) and (20) describe the coupling between radiator ion and plasma particles. For a vanishing radiator-plasma coupling, e.g. for a neutral radiator the pair correlation functions behave like  $g_{\alpha R} \rightarrow 1$ . If the radiator is a particle of plasma species  $\beta$  these correlations functions coincide with the radial distribution functions (RDF) of bulk plasma,  $g_{\alpha R} \equiv g_{\alpha\beta}$ .

The second moment for the regularized Coulomb interaction (see Eq. (3)) is with  $\tilde{u}_\alpha(r) = (r/\delta_{\alpha R}^2) e^{-r/\delta_{\alpha R}}$

$$\langle E^2 \rangle = \frac{k_B T n_e}{Z_R \varepsilon_0} \left[ \frac{1}{\delta_{eR}^2} \int_0^\infty e^{-r/\delta_{eR}} g_{eR}(r) r dr - \frac{1}{\delta_{iR}^2} \int_0^\infty e^{-r/\delta_{iR}} g_{iR}(r) r dr \right]. \quad (21)$$

Using a bare Coulomb interaction  $\tilde{u}_\alpha(r) = \delta(r)$  in Eq. (18) one recovers the result obtained in Ref. [42]

$$\langle E^2 \rangle = \frac{k_B T n_e}{Z_R \varepsilon_0} [g_{eR}(0) - g_{iR}(0)], \quad (22)$$

which can also be obtained from Eq. (21) by taking the limits  $\delta_{eR} \rightarrow 0$ ,  $\delta_{iR} \rightarrow 0$ . For  $Z_R > 0$ , we may assume that  $g_{iR}(0) = 0$  if quantum-diffraction effects are negligible for the ions, while  $g_{eR}(r)$  diverges at small distances for a bare Coulomb potential. This indicates that the second moment of the microfield distribution does not exist for a classical Coulomb TCP. But in the OCP limit  $g_{eR}(0) = 1$  one recovers the result  $\langle E^2 \rangle_{\text{OCP}} = k_B T Z n_i / Z_R \varepsilon_0$  for the classical (ionic) OCP [21].

#### IV. APPROXIMATE CALCULATIONS OF THE MFD

In this section we generalize the existing theoretical approaches developed originally for a OCP to a two component electron-ion plasma. For practical applications we will consider the exponential approximation considered in Ref. [46], and, as a simple but useful example the Holtsmark limit for the MFD in a TCP.

##### A. Ideal plasmas: Holtsmark distribution

We first consider the microfield distribution in an ideal TCP with  $\Gamma_{ee}, \Gamma_{ei}, \Gamma_{ii} \rightarrow 0$ , i.e. in the high temperature regime  $T \rightarrow \infty$ . In this case Eq. (12) yields

$$T(K) = \prod_\alpha \left\{ 1 - \frac{4\pi n_\alpha}{N_\alpha} \int_\Omega [1 - j_0(KE_\alpha(r))] r^2 dr \right\}^{N_\alpha}. \quad (23)$$

In the thermodynamic limit ( $N_\alpha, \Omega \rightarrow \infty$ ,  $N_\alpha/\Omega = n_\alpha = \text{const}$ ), and recalling that  $T(K) = e^{-\mathcal{L}(K)}$  we obtain from Eq. (23)

$$\mathcal{L}(K) = \sum_\alpha 4\pi n_\alpha \int_0^\infty [1 - j_0(KE_\alpha(r))] r^2 dr. \quad (24)$$

We study this expression for two types of interaction potentials.

(i) For a bare Coulomb interaction Eq. (24) yields  $\mathcal{L}(K) = (KE_H)^{3/2}$ , where  $E_H$  is the Holtsmark field for a TCP,  $E_H^{3/2} = E_{He}^{3/2} + E_{Hi}^{3/2}$ . Here  $E_{He}$  and  $E_{Hi}$  are the electronic and ionic Holtsmark fields, respectively,  $E_{He} = Ce_F/a_e^2$ ,  $E_{Hi} = CZe_F/a_i^2$  with  $C = (8\pi/25)^{1/3}$ . Since  $E_{He} = Z^{-1/3}E_{Hi}$  the electronic and ionic components of a hydrogen TCP contribute equally to the Holtsmark field. For a completely ionized TCP with highly charged ions the ions dominate  $E_H$ . The definition of

the Holtsmark field  $E_H$  for a TCP is equivalent to the obvious relation  $n = n_e + n_i$  and can be represented as

$$E_H = \left(\frac{8\pi}{25}\right)^{1/3} \frac{\mathcal{Z}e_F}{a^2} = \left(\frac{8\pi}{25}\right)^{1/3} \frac{e_F}{a^2} \left[ \frac{Z(1+Z^{1/2})}{Z+1} \right]^{2/3} \quad (25)$$

with an effective charge  $\mathcal{Z}$ . For a hydrogen TCP with  $Z = 1$  also  $\mathcal{Z} = 1$ . In other cases the effective charge increases with  $Z$  and behaves as  $\mathcal{Z} = Z^{1/3}$  for large  $Z$ . Thus the ideal two-component plasma can be regarded as an ionic OCP with effective ionic charge  $\mathcal{Z}$ .

Since the function  $\mathcal{L}(K)$  has a singularity at  $K = 0$  it cannot be expanded there and the second moment does not exist. The microfield distribution is given by  $P_H(E) = H(\eta)/E_H$  in terms of Holtsmark's function  $H(\eta)$

$$H(\eta) = \frac{2\eta}{\pi} \int_0^\infty e^{-x^{3/2}} \sin(\eta x) dx \quad (26)$$

with  $\eta = E/E_H$ . Note that the Holtsmark distribution for the TCP has the same functional form as either the ionic or the electronic OCP. The only difference is the definition of the Holtsmark field. Since the electronic or ionic Holtsmark fields may significantly differ from  $E_H$  the shape of the MFD for a OCP and a TCP may strongly differ from each other even for ideal plasmas.

(ii) For the regularized Coulomb interaction given by Eq. (3),  $\mathcal{L}(K)$  (from Eq. (24)) and all its derivatives are regular at  $K = 0$ . Hence, all moments of the microfield distribution exist. This indicates that for large electric fields the microfield distribution must decay exponentially. The second moment can be obtained from Eq. (24) if we recall that for  $K \rightarrow 0$ ,  $\mathcal{L}(K) \simeq (K^2/6) \langle E^2 \rangle$ , thus

$$\langle E^2 \rangle = 2\pi n_e e_F^2 \left( \frac{1}{\delta_{eR}} + \frac{Z}{\delta_{iR}} \right). \quad (27)$$

For large electric fields the main contribution to the microfield distribution comes from small  $K$  and we obtain the asymptotic behavior

$$P(E) \simeq 3\sqrt{\frac{6}{\pi}} \frac{E^2}{\langle E^2 \rangle^{3/2}} \exp\left(-\frac{3E^2}{2\langle E^2 \rangle}\right), \quad (28)$$

where  $\langle E^2 \rangle$  is given by Eq. (27). For large  $K$  ( $K \rightarrow \infty$ ) the function  $\mathcal{L}(K)$  (Eq. (24)) behaves as for the bare Coulomb interaction  $\mathcal{L}(K) \simeq (KE_H)^{3/2}$ . Hence, the microfield distributions for the ideal plasmas with bare and regularized Coulomb potentials behave similar at small electric fields.

## B. Expression of the MFD through pair functions

It was first noted by Morita [27] that the virial expansion of the Fourier transform of the MFD  $T(\mathbf{K})$  is formally similar to that of the excess chemical potential. This was previously used to

express  $T(\mathbf{K})$  in terms of an effective RDFs (see, e.g., [26]) involving the radiator and one of the plasma particles. To generalize this method to the TCP we follow the procedure [6-30] and consider the logarithmic derivative of Eq. (12)

$$-\frac{\partial \mathcal{L}(\mathbf{K})}{\partial K} = i \frac{\langle (\hat{\mathbf{K}} \cdot \mathbf{E}) e^{i\mathbf{K} \cdot \mathbf{E}} \rangle}{\langle e^{i\mathbf{K} \cdot \mathbf{E}} \rangle} = i \hat{\mathbf{K}} \cdot \sum_{\alpha} n_{\alpha} \int d\mathbf{r} \mathbf{E}_{\alpha}(\mathbf{r}) [\mathcal{G}_{\alpha R}(\mathbf{r}, \mathbf{K}) - 1]. \quad (29)$$

Here  $\mathbf{E}_e(\mathbf{r})$  and  $\mathbf{E}_i(\mathbf{r})$  are the single-particle electronic and ionic electrical fields introduced above, and  $\hat{\mathbf{K}}$  is a unit vector in the direction of  $\mathbf{K}$ .  $\mathcal{G}_{eR}(\mathbf{r}, \mathbf{K})$  and  $\mathcal{G}_{iR}(\mathbf{r}, \mathbf{K})$  represent the pair correlation functions between the radiator and the plasma particles in a fictitious system whose interaction potential is given by the complex quantity  $\mathcal{U}(\mathcal{T}_e, \mathcal{T}_i, \mathbf{K}) = U(\mathcal{T}_e, \mathcal{T}_i) - i(k_B T)(\mathbf{K} \cdot \mathbf{E})$ , i.e.,

$$\mathcal{G}_{eR}(\mathbf{r}_1, \mathbf{K}) = \frac{\Omega^2}{\mathcal{W}(\mathbf{K})} \int_{\Omega} e^{-\beta_T \mathcal{U}(\mathcal{T}_e, \mathcal{T}_i, \mathbf{K})} d\mathcal{T}_e^{(1)} d\mathcal{T}_i, \quad (30)$$

$$\mathcal{G}_{iR}(\mathbf{r}_1, \mathbf{K}) = \frac{\Omega^2}{\mathcal{W}(\mathbf{K})} \int_{\Omega} e^{-\beta_T \mathcal{U}(\mathcal{T}_e, \mathcal{T}_i, \mathbf{K})} d\mathcal{T}_e d\mathcal{T}_i^{(1)} \quad (31)$$

with the generalized, reduced partition function  $\mathcal{W}(\mathbf{K}) \equiv \mathcal{W}(K) = W \langle e^{i\mathbf{K} \cdot \mathbf{E}} \rangle$ . It can be easily checked that this function is real. In general these correlation functions are complex and satisfy the symmetry relations  $\mathcal{G}_{\alpha R}(-\mathbf{r}, \mathbf{K}) = \mathcal{G}_{\alpha R}^*(\mathbf{r}, \mathbf{K})$  and  $\mathcal{G}_{\alpha R}(-\mathbf{r}, -\mathbf{K}) = \mathcal{G}_{\alpha R}(\mathbf{r}, \mathbf{K})$ , where the asterisk denotes the complex conjugate. The correlation functions in the fictitious system are not spherical symmetric. At  $\mathbf{K} = 0$  they coincide with  $g_{\alpha R}(r)$  given by Eqs. (19) and (20). The complex correlation functions  $\mathcal{G}_{\alpha R}$  can be expressed through two functions  $\mathcal{G}_{\alpha R}^{(0)}(r, K)$  and  $\mathcal{E}_{\alpha}^{(0)}(\mathbf{r}, K) = \hat{\mathbf{r}} \mathcal{E}_{\alpha}^{(0)}(r, K)$ ,

$$\mathcal{G}_{\alpha R}(\mathbf{r}, \mathbf{K}) = \mathcal{G}_{\alpha R}^{(0)}(r, K) \exp \left[ i \mathbf{K} \cdot \mathcal{E}_{\alpha}^{(0)}(\mathbf{r}, K) \right], \quad (32)$$

where  $\mathcal{G}_{\alpha R}^{(0)}(r, K)$  and  $\mathcal{E}_{\alpha}^{(0)}(r, K)$  are spherical symmetric real functions. With this choice the functions  $\mathcal{G}_{\alpha R}(\mathbf{r}, \mathbf{K})$  automatically satisfy the symmetry relations. In the limit  $\mathbf{K} \rightarrow 0$ , we have also  $\mathcal{G}_{\alpha R}^{(0)}(r, 0) = g_{\alpha R}(r)$ . Inserting Eq. (32) into Eq. (29), integrating over  $K$  and taking into account that  $\mathcal{L}(0) = 0$  we obtain

$$\mathcal{L}(K) = 4\pi \sum_{\alpha} n_{\alpha} \int_0^{\infty} E_{\alpha}(r) r^2 dr \int_0^K \mathcal{G}_{\alpha R}^{(0)}(r, \lambda) j_1(\lambda \mathcal{E}_{\alpha}^{(0)}(r, \lambda)) d\lambda, \quad (33)$$

where  $j_1(x) = -j_0'(x)$ . Eq. (33) is an exact result which allows to express the MFD through complex pair correlation functions (or, alternatively through two real functions). In addition Eq. (33) yields the exact second moment given by Eq. (18).

The problem is now the evaluation of these correlation functions. Eq. (33) requires that the complex correlation functions has to be known in the interval from 0 to  $K$ . One possibility is to

apply the integral equation technique with the complex interaction energy introduced above. Such an approach has been previously employed for a OCP [28, 29, 30] and shows good agreement with computer simulations. Here we adopt the exponential approximation (see, e.g., [21, 22, 23, 24, 25, 26, 46]) and generalize it to the TCP. This method is based on thermodynamic perturbation theory [47]. The system with the potential energy  $\mathcal{U}(K = 0) = U$  is chosen as reference system and its structure is assumed to be known to a good approximation. The perturbation potential is then given by  $U_1 = -i(k_B T)(\mathbf{K} \cdot \mathbf{E})$  and we expand the correlation functions, Eqs. (30) and (31), with respect to  $U_1$ . Within first order we obtain  $\mathcal{G}_{\alpha R}(\mathbf{r}, \mathbf{K}) \simeq g_{\alpha R}(r)[1 + i\mathbf{K} \cdot \mathcal{E}_\alpha(\mathbf{r})]$ . Here  $g_{\alpha R}(r)$  are the actual RDF in the real system, Eqs. (19) and (20), and  $\mathcal{E}_\alpha(\mathbf{r}) = \mathcal{E}_\alpha^{(0)}(\mathbf{r}, 0)$ . The electric fields  $\mathcal{E}_\alpha(\mathbf{r})$  may be interpreted as effective electric fields in the fictitious system which are independent of  $\mathbf{K}$ . Taking into account that  $\langle \mathbf{E} \rangle = 0$  we obtain

$$\mathcal{E}_\alpha(\mathbf{r}) = \mathbf{E}_\alpha(\mathbf{r}) + \frac{1}{g_{\alpha R}(r)} \sum_\beta n_\beta \int d\mathbf{r}_1 \mathbf{E}_\beta(\mathbf{r}_1) [g_{\alpha\beta}(|\mathbf{r} - \mathbf{r}_1|) - 1]. \quad (34)$$

Comparing Eq. (34) with Eq. (3.8) of Ref. [21] for the case of a OCP we remark that our present derivation yields an additional factor  $1/g_{\alpha R}(r)$  in front of the second term. Since  $g_{\alpha\beta}(r)$  depend only on  $|\mathbf{r}_1 - \mathbf{r}_2|$  the effective electric fields in Eq. (34) can be represented as  $\mathcal{E}_\alpha(\mathbf{r}) = \hat{\mathbf{r}}\mathcal{E}_\alpha(r)$ . The  $\mathcal{E}_\alpha(r)$  can be expressed by the pair correlation functions and the single-particle potentials  $u_{\alpha R}(r)$  (see Appendix A for details). Alternatively the Fourier transformed single-particle electric fields can be written as  $\mathbf{E}_\alpha(\mathbf{k}) = \hat{\mathbf{k}}E_\alpha(k)$  which allows to express the effective fields through the static structure factors  $S_{\alpha\beta}(k)$ .

We make now the ansatz,

$$\mathcal{G}_{\alpha R}(\mathbf{r}, \mathbf{K}) = g_{\alpha R}(r) \exp[i\mathbf{K} \cdot \mathcal{E}_\alpha(\mathbf{r})] \quad (35)$$

and then integrate Eq. (33) with respect to  $\lambda$ , to find

$$\mathcal{L}(K) = \sum_\alpha 4\pi n_\alpha \int_0^\infty E_\alpha(r) \frac{1 - j_0(K\mathcal{E}_\alpha(r))}{\mathcal{E}_\alpha(r)} g_{\alpha R}(r) r^2 dr. \quad (36)$$

The second moment within the exponential approximation can be found from Eq. (36) at  $K \rightarrow 0$  and results in

$$\langle E^2 \rangle = \sum_\alpha 4\pi n_\alpha \int_0^\infty E_\alpha(r) \mathcal{E}_\alpha(r) g_{\alpha R}(r) r^2 dr. \quad (37)$$

This must fulfill the exact second moment of the MFD given by Eq. (18) or (33), which is not affected by either the assumption (35) or its first order Taylor expansion with respect to  $\mathbf{K}$ .

The APEX approach was originally developed for the classical ionic OCP with bare Coulomb interaction. In order to fulfill the exact second moment  $\langle E^2 \rangle_{\text{OCP}} = k_B T Z n_i / Z_R \varepsilon_0$ , Eq. (37) must take the form

$$\int_0^\infty \mathcal{E}(r) g_R(r) dr = \frac{k_B T}{Z_R e}. \quad (38)$$

In Ref. [21] the effective field  $\mathcal{E}(r)$  is assumed as a Debye-Hückel like screened interaction with unknown screening length. This free parameter is then adjusted in such a way to satisfy Eq. (38). The resulting predictions of APEX for the probability densities show excellent agreement with numerical simulation data for the OCP. However, difficulties appear when one attempts to extend the APEX scheme to a TCP, e.g. by assuming a Debye-Hückel like interaction separately for the electrons and the ions and introducing two adjustable screening lengths. Then the sum rule Eq. (38) with the exact second moment  $\langle E^2 \rangle$  becomes ambiguous as it allows for many different choices of the adjustable screening lengths. This can be cured for ionic mixtures by demanding that the second moment rule is satisfied species by species (see, e.g., [23, 24]). But this cannot be employed for a TCP with attractive electron-ion interactions. Here the Debye-Hückel ansatz for the electronic effective field is physically incompatible with Eq. (37) as discussed in Ref. [42].

We instead apply the potential of mean force (PMF) approximation [42, 48] which expresses the effective electric fields through the logarithmic derivative of pair correlation functions

$$\mathcal{E}_\alpha(r) = \frac{k_B T}{Z_R e} \frac{\partial}{\partial r} [\ln g_{\alpha R}(r)]. \quad (39)$$

Introducing Eqs. (39) in Eq. (37) automatically satisfies the sum-rule (18) without any adjustable parameter. Relations (39) can be deduced from Eqs. (19), (20) and (34). To show this we consider the pair correlation functions given by Eqs. (19) and (20). It is clear that in the thermodynamic limit these expressions are translationally invariant with respect to  $\mathbf{r}_a^{(\alpha)} \rightarrow \mathbf{r}_a^{(\alpha)} + \mathbf{r}_1^{(\alpha)}$  ( $a = 2, 3, \dots, N_\alpha$ ). Making these transformations and calculating the logarithmic derivatives of the pair correlation functions yield Eq. (39), where the effective fields are given by Eq. (34). In addition, Eq. (39) can be interpreted as a integro-differential equation for determining the pair correlation functions,  $g_{\alpha R}$ . Thus, if the  $g_{\alpha R}(r)$  are known the MFD with the exact second moment can be calculated using Eqs. (13), (36) and (39). This approach based on the exponential and the PMF approximations is abbreviated as PMFEX in the following.

We summarize this section by the following remarks. The possibilities of the PMF approximation have already been noted by Alastuey *et al.* [22]. They found a superiority of the APEX to the PMF approximation since the former reproduces the simulation data for classical ionic OCP

more accurately than the latter. We have confirmed this by own investigations on the OCP. For the TCP the outlined PMFEX approximation agrees quite well with the MD simulation results, as we will show in the next section.

## V. RESULTS

In Sec. IV we introduced and outlined the PMFEX approximation which links the MFD to the RDFs. To obtain explicit results for the MFD the corresponding RDFs have to be determined first. This will be done by solving numerically the Hyper-Netted-Chain (HNC) integral equations for the TCPs under consideration. The HNC method and the PMFEX approximation are tested both by comparison of the resulting RDFs and MFD with those obtained by classical MD simulations. We have done that for a wide range of coupling parameters  $\Gamma_{ei}$  and for two specific rather distinct cases  $H^+$  ( $n_e = n_i$ ) and  $Al^{13+}$  ( $n_e = 13n_i$ ) TCPs with symmetric and asymmetric density distributions between plasma species, respectively. For simplicity we assume bare Coulomb electron-electron and ion-ion interactions with  $\delta_{ee} \simeq 0$  and  $\delta_{ii} \simeq 0$  while the parameter  $\delta_{ei}/a = \bar{\delta}$  scaled in the Wigner-Seitz radius  $a = [4\pi(n_e + n_i)/3]^{-1/3}$  varies from 0.1 to 0.4.

### A. Numerical treatments

To determine the RDFs  $g_{\alpha R}(r)$  the HNC equations (see, e.g., Refs. [48, 49])

$$1 + h_{\alpha\beta}(r) = \exp [h_{\alpha\beta}(r) - c_{\alpha\beta}(r) - \beta_T q_\alpha q_\beta e_S^2 u_{\alpha\beta}(r)], \quad (40)$$

and the Ornstein-Zernike equations

$$h_{\alpha\beta}(r) = c_{\alpha\beta}(r) + \sum_\sigma n_\sigma \int d\mathbf{r}' c_{\alpha\sigma}(|\mathbf{r} - \mathbf{r}'|) h_{\sigma\beta}(r') \quad (41)$$

for the total correlation functions  $h_{\alpha\beta}(r) = g_{\alpha\beta}(r) - 1$  and the direct correlation functions  $c_{\alpha\beta}(r)$  are considered. This has to be done for a three-component system of electrons, ions and the radiator in general. Here we assume that the radiator is one of the plasma ions  $Z_R = Z$ , i.e.  $g_{\alpha R}(r) \rightarrow g_{\alpha i}(r)$ , which reduces Eqs. (40) and (41) to the HNC-scheme for a TCP with mutual interactions  $u_{\alpha\beta}(r)$  (see Eq. (3)). The resulting coupled equations (40) and (41) are solved numerically by an iterative scheme which closely follows the implementation discussed in detail in Ref. [50]. Within our numerical treatment a parameter regime with  $\sigma_{ei} = \sigma = \Gamma_{ei}/\bar{\delta} < \sigma_c(Z, \bar{\delta})$  is accessible, where the critical value  $\sigma_c$  for  $\bar{\delta} = 0.1, 0.2$  and  $0.4$  takes the values  $\sigma_c \simeq 8.32, 8.5, 13.4$  and  $\sigma_c \simeq 7.33, 6.66, 7.0$

for  $\text{H}^+$  and  $\text{Al}^{13+}$  TCPs, respectively. Beyond this value the numerical procedure does either not converge or ends up in unphysical solutions. A similar behavior has been reported in [43] for the case of an ion embedded in electrons. With the RDFs provided by the HNC-scheme the MFD, i.e.  $P(E)$ , is then calculated via Eqs. (13), (36) and (39) by standard numerical differentiation and integration methods [51].

In the MD simulations the classical equations of motion are numerically integrated for  $N_i$  ions and  $N_e$  electrons interacting via  $u_{\alpha\beta}(r)$  and contained in a cubic cell with periodic boundary conditions. To account for the long range of the Coulomb interaction the forces are calculated by an Ewald sum [52, 53]. The numerical propagation is accomplished by a standard Velocity-Verlet algorithm [54, 55] extended by a hierarchical treatment of close colliding particles which are propagated as subsystems (see [56] for details) and using an adaptive time step. Such MD simulations have already been extensively tested and successfully applied for investigations of the dynamic response of a TCP with regularized potentials, see [57, 58].

The actual simulations run with  $N = N_i + N_e = 2002$  particles and proceed in two phases. An initial equilibration starts from a random sampling of positions and velocities and relaxes towards the equilibrium distribution of desired temperature by dynamic propagation with velocity rescaling. The subsequent simulations are performed in the microcanonical ensemble, where their accuracy and stability can be monitored using the total energy. The MFD and the RDFs are sampled during the simulations from the known forces on the particles and their positions as a time average over the total running time  $\tau$  which was typically  $\tau \approx 700\omega_{\text{pl},e}^{-1}$ , where  $\omega_{\text{pl},e} = (n_e e^2 / m \epsilon_0)^{1/2}$  is the electronic plasma frequency.

By the MD simulations basically all correlations and many-body effects of classical many-body systems can be taken into account. Limitations arise mainly from the finite particle number and the system size, e.g. in connection with the screening of the interactions on a typical screening length  $\lambda_D$ . Since  $\lambda_D$  should be smaller than the size  $L$  of the simulation box and  $L/\lambda_D \propto \Gamma_{ei}^{1/2}$ , the MD-technique works here more favorable at large coupling ( $\Gamma_{ei} > 1$ ) while the limit of weak coupling ( $\Gamma_{ei} \ll 1$ ) requires a strong increase of the simulation box, i.e. of the particle number.

## B. Correlation functions

In Figs. 1-3 we compare the RDFs calculated either from the HNC scheme or MD simulations for a  $\text{H}^+$ -plasma. Only  $g_{ei}(r)$  and  $g_{ii}(r)$  are plotted as  $g_{ee}(r) = g_{ii}(r)$  for hydrogen both in the HNC and MD treatment (within numerical fluctuations). In Fig. 1 we explore the dependence in

the regularization parameter  $\delta$  at a fixed electron-electron coupling  $\Gamma_{ee} = 0.1$ , while in Fig. 2  $\Gamma_{ee}$  is varied. Both approaches agree perfectly in the range of parameters covered in these figures. Due to the regularization of the ion-electron interaction the RDF  $g_{ei}(r)$  is finite in the limit  $r \rightarrow 0$ . A non-linear Debye-Hückel approximation for  $g_{ei}(r)$  has been proposed in Ref. [43]. Adopting this estimate for TCPs we obtain  $g_{ei}(0) \simeq \exp(\Gamma_{ei}/\mathcal{R}\bar{\delta})$  with  $\mathcal{R} = 1 + \bar{\delta}(3\Gamma_{ei})^{1/2}$ , where the dependence on the ion charge  $Z$  is included in the coupling parameter  $\Gamma_{ei}$ . The RDFs show indeed the expected growth of correlations with increased coupling and decreased regularization parameter. For very strong electron-electron coupling deviations between the HNC scheme and the MD simulations begin to appear as shown in Fig. 3 for  $\Gamma_{ee} = 4.0$  and  $\sigma_{H^+} \simeq 12.5$ . There we are at the edge of the HNC convergence region and classically bound states show up in the MD simulations.

The symmetry between the correlation functions  $g_{ee}(r)$  and  $g_{ii}(r)$  breaks down for  $Al^{13+}$ -plasma. In Fig. 4 we compare the HNC and MD radial distribution functions for fixed  $\Gamma_{ee} = 0.01$  varying the regularization parameter  $\delta$ . Since  $\Gamma_{ii} \gg \Gamma_{ee}$  strong correlation effects are expected for  $g_{ii}$ . The increasing "correlation hole" is clearly visible in Fig. 5 where the HNC and MD radial distribution functions  $g_{ii}(r)$  and  $g_{ei}(r)$  are plotted for a fixed  $\bar{\delta} = 0.4$  and varying coupling strengths  $\Gamma_{ee}$ . Again, for all these parameters the HNC scheme agrees perfectly with the MD simulations. As shown in Fig. 6 deviations occur in the electron-electron RDF  $g_{ee}(r)$  at small  $r$  for strong coupling  $\Gamma_{ee} = 0.2$ ,  $\sigma_{Al^{13+}} \simeq 6.6$ . These are due to the enhancement of the electronic density around an ion, which also increases the probability of close electronic distances and results in the maxima in  $g_{ee}$  at distances  $r \lesssim a$ . This effect is obviously overestimated in the HNC approach and it is more pronounced for highly charged ions like  $Al^{13+}$  and less important for  $H^+$ . The regularization of the electron-ion interaction has no visible influence on the correlation functions  $g_{ee}(r)$  and  $g_{ii}(r)$  (see Figs. 1 and 4).

### C. Microfield distribution

We now turn to the MFDs at the charged reference point which is chosen to be one of the plasma ions,  $Z_R = Z$ . For our analysis it is instructive to consider first the second moment which can be used to check and compare the different treatments PMFEX, HNC, MD, and can provide some information about the shape of the MFD, although this is not sufficient to construct it. For a bare ion-ion Coulomb interaction the second term in the rhs of Eq. (21) vanishes and the second moment  $\langle E^2 \rangle$  receives contribution only from the first term involving  $g_{ei}$ . In the limit of an ideal TCP ( $\Gamma_{\alpha\beta} \rightarrow 0$ )  $g_{ei}(r)$  can be replaced by unity. This yields  $\langle E^2 \rangle_0 = k_B T n_e / Z \varepsilon_0 = (3/\Gamma_{ii}) E_{0i}^2 = (3/Z^{5/3} \Gamma_{ee}) E_{0i}^2$  with  $E_{0i} = Ze_F/a_i^2$  which is similar to the second moment obtained for the ionic

OCP (see, e.g., [21]). In this sense the ideal TCP behaves like an ionic OCP with  $\Gamma = \Gamma_{ii}$ . The second moments calculated from Eq. (21) using a HNC radial distribution function  $g_{ei}(r)$  are shown in Figs. 7 and 8 as a function of  $\Gamma_{ee}$  for hydrogen and aluminum TCPs, respectively. The dashed straight lines represent  $\langle E^2 \rangle_0$  for the ideal system. The other curves are calculated for different  $\delta$  up to the critical values  $\sigma_c = \Gamma_{ei}^{(c)}/\bar{\delta} = \left(\Gamma_{ee}^{(c)}/\bar{\delta}\right)(Z^2(Z+1))^{1/3}$  introduced above. For small  $\Gamma_{ee}$  the deviations of the second moment from  $\langle E^2 \rangle_0$  are small and the second moment decreases approximately as  $1/\Gamma_{ee}$ . But unlike  $\langle E^2 \rangle$  of an ionic OCP, it increases again with the coupling parameter  $\Gamma_{ee}$  due to the strong attractive ion-electron interactions.

The normalized MFDs from PMFEX and MD are compared in Figs. 9-18 where the electric microfields are scaled in units of the Holtsmark field  $E_H$  (see Eq. (25)). For each distribution we have also calculated the second moment as a control parameter and found a quite good agreement between Eq. (21) and the MD simulations. The MFDs for hydrogen with coupling parameters  $\Gamma_{ee} = \Gamma_{ii} = 1$  and for  $\text{Al}^{13+}$  plasmas with  $\Gamma_{ee} = 0.1$  and  $\Gamma_{ii} = 7.19$  are shown in Fig. 9 and 10, respectively. The dashed curves are the Holtsmark MFDs for a TCP with regularized Coulomb potential. Note that the Holtsmark MFD is  $Z$ -dependent here (see Eqs. (13) and (24)). To demonstrate the importance of attractive interactions we also plotted the MFDs  $P_0(E)$  resulting from the corresponding electronic and ionic OCPs with  $\Gamma_{ee}$  and  $\Gamma_{ii}$ , respectively (open circles). To that end the distribution  $Q_0(\mathbf{E})$  of the total field  $\mathbf{E} = \mathbf{E}_1 + \mathbf{E}_2$  is calculated as

$$Q_0(\mathbf{E}) = \int Q_e(\mathbf{E}_1) Q_i(\mathbf{E}_2) \delta(\mathbf{E} - \mathbf{E}_1 - \mathbf{E}_2) d\mathbf{E}_1 d\mathbf{E}_2 \equiv \frac{P_0(E)}{4\pi E^2} \quad (42)$$

from the MFD of the ionic OCP at a charged point  $Q_i(\mathbf{E}_2)$  and of the electronic OCP at a neutral reference point  $Q_e(\mathbf{E}_1)$ . The distribution  $Q_0(\mathbf{E})$  thus represents the MFD in a TCP assuming that the ion-electron attractive interaction is switched off. Here  $Q_e(\mathbf{E}_1)$  and  $Q_i(\mathbf{E}_2)$  are taken from MD simulations of an OCP.

Systematic dependencies of the MFD on  $\delta$  and  $\Gamma$  are shown in Figs. 11-16. For fixed  $\Gamma$  the maximum of  $P(E)$  shifts only slightly to lower field strengths  $E$  with increasing  $\delta$ , see Figs. 11 and 12, while the maximum itself increases with  $\delta$ . This is related to the largest possible single-particle field  $|E_e(0)| = e_F/2\delta^2$ , which an electron can produce at the ion. Thus the nearest neighbor electronic MFD vanishes for electric fields larger than  $|E_e(0)|$ , and smaller  $\delta$  will result in larger contributions to  $P(E)$  at higher fields  $E$  with a corresponding reduction of  $P(E)$  at small fields. In order to demonstrate the enhanced probability of large fields at small  $\delta$  and the behavior of PMFEX and MD treatments at large fields, the MFD is plotted in Figs. 13 and 14 in a double-logarithmic manner. From Fig. 13 it can be deduced that the behavior of the MFD at large fields in  $\text{H}^+$  plasma

with  $\bar{\delta} = 0.2$  and  $\Gamma_{ee} = 1$  is similar to the nearest neighbor electronic distribution considered in detail in Ref. [43]. In this case the MFD is strongly reduced at  $E > |E_e(0)| \simeq 12.5E_H$ .

For fixed  $\delta$  and increasing  $\Gamma$  the MFDs for hydrogen (Fig. 15) and  $\text{Al}^{13+}$  (Fig. 16) show different behavior. For hydrogen, like for an ionic OCP, the growing correlations shift the maximum of the MFD towards lower electric fields. In the  $\text{Al}^{13+}$ -TCP,  $P(E)$  first follows this trend, but then, for further increasing  $\Gamma$ , the maximum turns back to higher field strengths. This can be attributed to the growing contribution of the attractive electron-ion interaction and close ion-electron configurations, which are particularly important for a TCP with highly charged ions. These dependencies are very well reproduced by the PMFEX predictions.

The agreement with the MD data is nearly perfect in most of the studied cases, both for the  $\text{H}^+$ -TCP and the  $\text{Al}^{13+}$ -TCP (Figs. 9-16). The PMFEX approximation remains accurate also up to high electric fields where the MD data are characterized by strong fluctuations (see Figs. 13 and 14). Deviations emerge only for strongly coupling situations with large  $\Gamma$  and  $\sigma$ . One example is the case of strongly coupled hydrogen with  $\Gamma_{ee} = 1$  and  $\bar{\delta} = 0.2$ , i.e.  $\sigma \simeq 6.3$  (dotted line and open triangles in Fig. 15, see also Fig. 13). Here PMFEX and MD results differ considerably, although the HNC treatment is accurate in this case (see Fig. 2). To understand this feature better we recall that within PMFEX the Fourier transformed MFD,  $T(K)$ , fulfills exactly the second moment relation (21) in the limit  $K \rightarrow 0$ . As discussed above only electrons contribute to the second moment since the role of ions is negligible (the second term in Eq. (21)). Because of Eq. (36) small values of  $K$  correspond to large values of the local electric field. One expects therefore that the PMFEX yields good results if there are many electrons near the ion. On the other hand, for a large electron-electron repulsion  $\Gamma_{ee} = 1$  and a light ion like hydrogen, the electrons tend to exert only small fields in the ion, for which the quality of the PMFEX is less obvious.

With increased coupling also the shape of the MFD starts to change. First by a broadening of the maximum, and then by the appearance of a shoulder as also reported in Ref. [43] which then gets more and more pronounced and finally develops into a second maximum. For the  $\text{Al}^{13+}$ -TCP in a parameter regime still below the critical values, the MFD is characterized here by the formation of the characteristic shape shown in Fig. 17. The HNC approximation still gives the correct  $g_{ii}(r)$  and  $g_{ei}(r)$  and the PMFEX well reproduces the broadening and the specific shape of the MFD. With respect to  $g_{ee}(r)$ , however, deviations between HNC and MD emerge (similar to those shown for  $\delta = 0.4a$ ,  $\Gamma_{ee} = 0.2$  in Fig. 6), although the electron-electron coupling ( $\Gamma_{ee} = 0.1$ ) is still small. The strong ion-electron coupling increases the electron density near the ion which introduces additional correlations between electrons, see the discussion above in Sec. VB. This

will, however, not affect the quality of the PMFEX approximation, since the  $g_{ee}(r)$  is not needed for the calculation of the MFD at the impurity ion (see Eqs. (13) and (36)). An example for a second maximum is given by the strongly coupled hydrogen of Fig. 18, where the parameters are close to the critical values. This regime is characterized by the population of bound states and the formation of a separate contribution to  $P(E)$  at high fields which is mainly due to the electrons. Here occur significant deviations between the HNC approach and MD simulations in the RDF  $g_{ei}(r)$  (see Fig. 3) and the PMFEX approximation cannot predict the shape of the MFD, even not qualitatively. But, for coupling parameters, where a classical approach is justified, i.e. when bound states are unimportant, the PMFEX approach turns out to be a very reliable method for calculating the MFD of a TCP with attractive interaction.

## VI. DISCUSSION AND CONCLUSION

In this paper our objective was to investigate the microfield distributions in a two-component plasmas with attractive electron-ion interactions. Attention has been focused on testing the predictions of the PMFEX approximation based on the HNC treatment of static correlations by confronting it with the MFDs obtained from MD simulations. One of the basic assumptions of the model considered here is the regularization of the attractive Coulomb interaction at short distances to introduce quantum diffraction effects in the employed classical approach.

Two specific rather distinct cases,  $\text{H}^+$  ( $n_e = n_i$ ) and  $\text{Al}^{13+}$  ( $n_e = 13n_i$ ) two-component plasmas with symmetric and largely asymmetric density distributions between plasma species were considered. For simplicity we assume bare Coulomb electron-electron and ion-ion interactions while the parameter  $\bar{\delta}$  for the regularized ion-electron potential varies from 0.1 to 0.4. The coupling strength between plasma particles is measured by the coupling parameters  $\Gamma_{\alpha\beta}$  with  $\alpha, \beta = e, i$  and by the ion-electron potential at the origin in units of  $k_B T$ ,  $\sigma = \Gamma_{ei}/\bar{\delta}$ . Our treatment is limited to a parameter regime with  $\sigma < \sigma_c(Z, \bar{\delta})$ , where the critical value  $\sigma_c$  for  $0.1 \leq \bar{\delta} \leq 0.4$  varies  $8.32 \leq \sigma_c \leq 13.4$  and  $6.66 \leq \sigma_c \leq 7.33$  for  $\text{H}^+$  and  $\text{Al}^{13+}$  TCPs, respectively. Within this parameter regime the  $g_{\alpha\beta}(r)$  from the HNC equations agree well with the MD simulations. Beyond these critical  $\sigma$  the HNC equations do either not converge or end up in unphysical solutions while the MD simulations remain effective at these strong coupling regimes. A further increase of the coupling parameters also leads to the formation of classical strongly bound electronic states with no corresponding quantum counterpart. Also the microfield distributions obtained from the HNC via the PMFEX approximation agree excellently with the MFDs from the MD simulations except

of some cases close to the critical  $\Gamma, \sigma$ . This is somewhat surprising since a similar approximation studied for the OCP deviates from MD simulations (see, e.g., [21, 22]). Therefore we have also tested the PMFEX approximation for an OCP, which in contrast to the TCP turns out to be poor when compared with MD simulations although the exact second moment is satisfied within the PMFEX. The success of the PMFEX approximation for the TCP is a consequence of the attractive interaction and is related to the additional positive electronic part in Eq. (36) which accounts for the electric fields created by the electrons at the ions. Obviously, the attractive interactions in a TCP favour configurations with large electric fields created at the ion which are well described within the PMFEX approximation. On the other hand, in a regime dominated by small local fields and hence by small local electronic density the PMFEX deviates from the MD. This feature has been clearly observed for a single ion embedded in an electronic OCP in Ref. [43]. For the TCP, an example is the case of strongly coupled hydrogen with  $\Gamma_{ee} = 1, \delta = 0.2a$  in Figs. 13 and 15. Here some improvement of the PMFEX scheme is required. Such work and the application of PMFEX to the case of a neutral radiator are in progress.

### Acknowledgments

This work was supported by the Bundesministerium für Bildung und Forschung (BMBF) under contract no 06ER128.

## APPENDIX A: THE EFFECTIVE ELECTRIC FIELDS

In order to reduce the three-dimensional integration in Eq. (34) to a one-dimensional integration and to express the effective fields through scalar potentials  $u_{\alpha R}(r)$  we consider the following expression

$$\int d\mathbf{r}_1 u_{\beta R}(r_1) [g_{\alpha\beta}(|\mathbf{r} - \mathbf{r}_1|) - 1] = 4\pi \int_0^\infty G_\beta^{(0)}(r, \rho) [g_{\alpha\beta}(\rho) - 1] \rho d\rho, \quad (A1)$$

where

$$G_\beta^{(0)}(r, \rho) = \frac{1}{2r} \int_{|r-\rho|}^{r+\rho} u_{\beta R}(r') r' dr'. \quad (A2)$$

Obviously, the gradient of Eq. (A1) yields the second term in Eq. (34). Consequently, recalling the spherical symmetry of the single particle fields, Eq. (34) can be alternatively expressed through one-dimensional integrals

$$\mathcal{E}_\alpha(r) = E_\alpha(r) + \frac{4\pi e_F}{g_{\alpha R}(r)} \sum_\beta q_\beta n_\beta \int_0^\infty G_\beta^{(1)}(r, \rho) [g_{\alpha\beta}(\rho) - 1] \rho d\rho. \quad (A3)$$

Here

$$G_{\beta}^{(1)}(r, \rho) = -\frac{\partial}{\partial r} G_{\beta}^{(0)}(r, \rho). \quad (\text{A4})$$

For the regularized Coulomb interaction the last expression yields for  $r < \rho$  and  $r > \rho$ , respectively

$$G_{\beta}^{(1)}(r, \rho) = \frac{\delta_{\beta R}}{r^2} e^{-\rho/\delta_{\beta R}} \left[ \frac{r}{\delta_{\beta R}} \operatorname{ch} \left( \frac{r}{\delta_{\beta R}} \right) - \operatorname{sh} \left( \frac{r}{\delta_{\beta R}} \right) \right], \quad (\text{A5})$$

$$G_{\beta}^{(1)}(r, \rho) = \frac{\delta_{\beta R}}{r^2} \left[ \frac{\rho}{\delta_{\beta R}} - \operatorname{sh} \left( \frac{\rho}{\delta_{\beta R}} \right) \left( 1 + \frac{r}{\delta_{\beta R}} \right) e^{-r/\delta_{\beta R}} \right]. \quad (\text{A6})$$

For bare Coulomb interaction Eqs. (A5) and (A6) for  $r < \rho$  and  $r > \rho$  are reduced to  $G_{\beta}^{(1)}(r, \rho) = 0$  and  $G_{\beta}^{(1)}(r, \rho) = \rho/r^2$ , respectively.

---

[1] H. R. Griem, *Spectral Line Broadening by Plasmas* (Academic Press, New York, 1974).

[2] D. Salzmann, *Atomic Physics in Hot Plasmas* (Oxford University Press, Oxford, 1998).

[3] See databases of bibliographic references on the Internet at <http://physics.nist.gov/PhysRefData/Linebr/html/reffrm0.html> (J. R. Fuhr, H. R. Felrice, and K. Olsen).

[4] Z. Jiang *et al.*, Phys. Plasmas **2**, 1702 (1995); D. Gilles and O. Peyrusse, J. Quant. Spectrosc. Radiat. Transf. **53**, 647 (1995).

[5] Y. Vitel, M. El Bezzari, L. G. Dyachkov, Yu. K. Kurilenkov, Phys. Rev. E **58**, 7855 (1998).

[6] J. Holtsmark, Ann. Phys. (Leipzig) **58**, 577 (1919).

[7] H. Margenau, Phys. Rev. **40**, 387 (1932).

[8] J. E. Mayer and M. G. Mayer, *Statistical Mechanics* (Wiley, New York, 1940).

[9] M. Baranger and B. Mozer, Phys. Rev. **115**, 521 (1959).

[10] B. Mozer and M. Baranger, Phys. Rev. **118**, 626 (1960).

[11] C. F. Hooper, Jr., Phys. Rev. **149**, 77 (1966);

[12] C. F. Hooper, Jr., Phys. Rev. **165**, 215 (1968).

[13] R. J. Tighe and C. F. Hooper, Jr., Phys. Rev. A **14**, 1514 (1976).

[14] R. J. Tighe and C. F. Hooper, Jr., Phys. Rev. A **15**, 1773 (1977).

[15] A. A. Broyles, Phys. Rev. **100**, 1181 (1955); Z. Physik **151**, 187 (1958);

[16] C. A. Iglesias and C. F. Hooper, Jr., Phys. Rev. A **25**, 1049 (1982).

[17] B. Held and C. Deutsch, Phys. Rev. A **24**, 540 (1981).

[18] A. Davletov and M.-M. Gombert, Phys. Rev. E **70**, 046404 (2004).

[19] H. Mayer, Los Alamos Scientific Laboratory Report No. LA-647, 1947 (unpublished).

- [20] C. A. Iglesias *et al.*, J. Quant. Spectrosc. Radiat. Transf. **65**, 303 (2000).
- [21] C. A. Iglesias, J. L. Lebowitz, and D. MacGowan, Phys. Rev. A **28**, 1667 (1983).
- [22] A. Alastuey, C. A. Iglesias, J. L. Lebowitz, D. Levesque, Phys. Rev. A **30**, 2537 (1984).
- [23] C. A. Iglesias, H. E. DeWitt, J. L. Lebowitz, D. MacGowan, W. B. Hubbard, Phys. Rev. A **31**, 1698 (1985).
- [24] C. A. Iglesias and J. L. Lebowitz, Phys. Rev. A **30**, 2001 (1984).
- [25] J. W. Dufty, D. B. Boercker, and C. A. Iglesias, Phys. Rev. A **31**, 1681 (1985).
- [26] C. A. Iglesias, Phys. Rev. A **27**, 2705 (1983).
- [27] T. Morita, Prog. Theor. Phys. **22**, 757 (1959); **23**, 1211 (1960).
- [28] F. Lado, Phys. Rev. A **34**, 4131 (1986).
- [29] F. Lado, Phys. Rev. A **36**, 313 (1987).
- [30] F. Lado and J. W. Dufty, Phys. Rev. A **36**, 2333 (1987).
- [31] D. Gilles and A. Angelie, Ann. Phys. (Paris) **11**, 157 (1986).
- [32] R. Stamm, B. Talin, E. L. Pollock, C. A. Iglesias, Phys. Rev. A **34**, 4144 (1986).
- [33] D. Gilles and C. Stehle, J. Phys. II **5**, 75 (1995).
- [34] J.-M. Caillol and D. Gilles, J. Stat. Phys. **100**, 905 (2000).
- [35] J. Marten and C. Toepffer, Eur. Phys. J. D **29**, 397 (2004).
- [36] A. V. Demura, D. Gilles, and C. Stehle, J. Quant. Spectrosc. Radiat. Transf. **54**, 123 (1995); C. Stehle, D. Gilles, and A. V. Demura, Eur. Phys. J. D **12**, 355 (2000).
- [37] M. S. Murillo, D. P. Kilcrease, and L. A. Collins, Phys. Rev. E **55**, 6289 (1997).
- [38] A. Alastuey, J. L. Lebowitz, and D. Levesque, Phys. Rev. A **43**, 2673 (1991).
- [39] Yu. K. Kurilenkov and V. S. Filinov, High Temp. **18**, 509 (1980).
- [40] C. F. Hooper, Jr., Phys. Rev. **169**, 193 (1968).
- [41] A. Y. Potekhin, G. Chabrier and D. Gilles, Phys. Rev. E **65**, 036412 (2002).
- [42] X.-Z. Yan and S. Ichimaru, Phys. Rev. A **34**, 2167 (1986).
- [43] B. Talin, A. Calisti, and J. Dufty, Phys. Rev. E **65**, 056406 (2002).
- [44] G. Kelbg, Ann. Phys. (Leipzig) **12**, 219 (1963); **13**, 354 (1964); **14**, 394 (1964).
- [45] C. Deutsch, Y. Furutani, and M. M. Gombert, Phys. Rep. **69**, 85 (1981); C. Deutsch, Phys. Lett. A **60**, 317 (1977); C. Deutsch, M.-M. Gombert, and H. Minoo, *ibid.* **66**, 381 (1978); H. Minoo, M.-M. Gombert, and C. Deutsch, Phys. Rev. A **23**, 924 (1981).
- [46] H. C. Andersen and D. Chandler, J. Chem. Phys. **57**, 1918 (1972).
- [47] R. W. Zwanzig, J. Chem. Phys. **22**, 1420 (1954).
- [48] J.-P. Hansen and I. R. McDonald, *Theory of Simple Liquids* (Academic, New York, 1976).
- [49] M. Baus and J. P. Hansen, Phys. Rep. **59**, 1 (1980).
- [50] T. Pschiwul, *Untersuchungen zu dielektrischen und Transporteigenschaften von nichtidealen Zweikomponentenplasmen* (Shaker Verlag, Aachen, 2004).
- [51] W. H. Press, B. P. Flannery, S. A. Teukolsky, and W. T. Vetterling, *Numerical Recipes* (Cambridge

University Press, Cambridge, 1989).

- [52] B. R. A. Nijboer and F. W. De Wette, *Physica* **23**, 309 (1957).
- [53] J. P. Hansen, *Phys. Rev. A* **8**, 3096 (1973).
- [54] L. Verlet, *Phys. Rev.* **159**, 98 (1967).
- [55] M. P. Allen and D. J. Tildesley, *Computer Simulation of Liquids* (Clarendon Press, Oxford, 1987).
- [56] G. Zwicknagel, C. Toepffer, and P.-G. Reinhard, *Phys. Rep.* **309**, 117 (1999).
- [57] T. Pschiwul and G. Zwicknagel, *J. Phys. A: Math. Gen.* **36**, 6251 (2003).
- [58] G. Zwicknagel and T. Pschiwul, *Contrib. Plasma Phys.* **43**, 393 (2003).

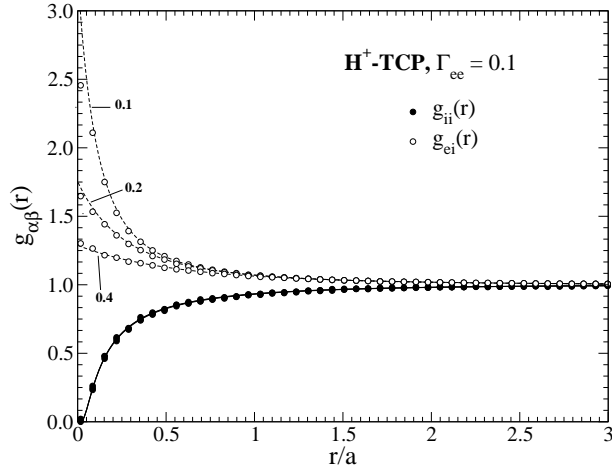


FIG. 1: RDFs  $g_{\alpha\beta}(r)$  for a  $H^+$  plasma with fixed  $\Gamma_{ee} = 0.1$  and  $\bar{\delta} = 0.1, 0.2$ , and  $0.4$ . The lines correspond to the HNC approximation while the symbols denote the MD simulations. The different lines and symbols represent  $g_{ii}^{\text{HNC}} \equiv g_{ee}^{\text{HNC}}$  (solid lines),  $g_{ei}^{\text{HNC}}$  (dashed lines),  $g_{ii}^{\text{MD}} = g_{ee}^{\text{MD}}$  (filled circles),  $g_{ei}^{\text{MD}}$  (open circles). The numbers indicate the values of  $\bar{\delta}$ .

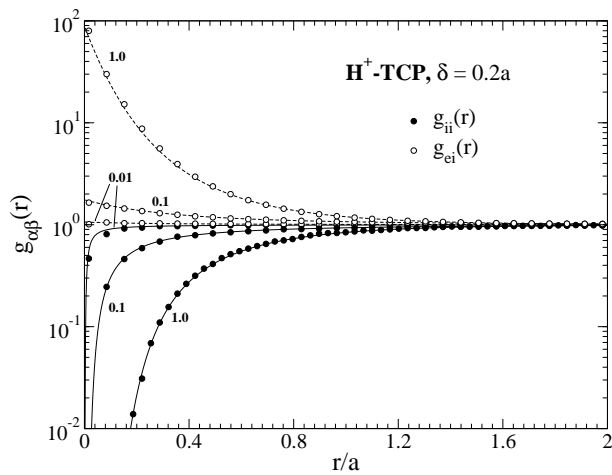


FIG. 2: Same as Fig. 1 with fixed  $\bar{\delta} = 0.2$  and  $\Gamma_{ee} = 0.01, 0.1$ , and  $1.0$ . Here the numbers indicate the values of  $\Gamma_{ee}$ .

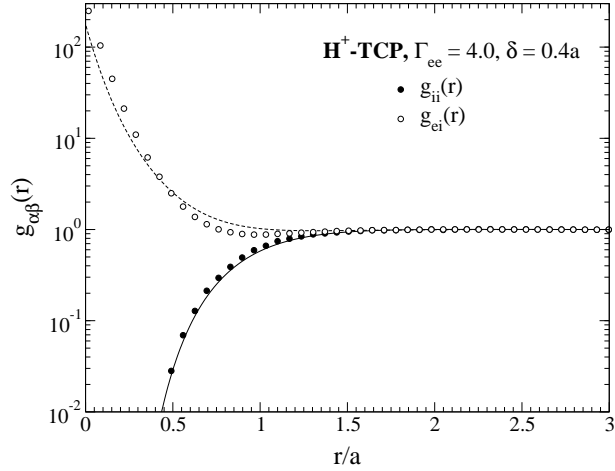


FIG. 3: Same as Fig. 1 for  $\Gamma_{ee} = 4.0$  and  $\bar{\delta} = 0.4$ .

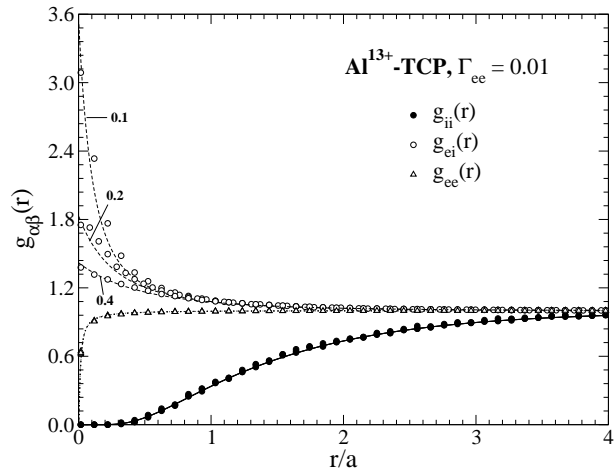


FIG. 4: Same as Fig. 1 for a  $\text{Al}^{13+}$  plasma with fixed  $\Gamma_{ee} = 0.01$  and  $\bar{\delta} = 0.1, 0.2$ , and  $0.4$ . The dotted lines and the triangles represent  $g_{ee}^{\text{HNC}}$  and  $g_{ee}^{\text{MD}}$ , respectively.

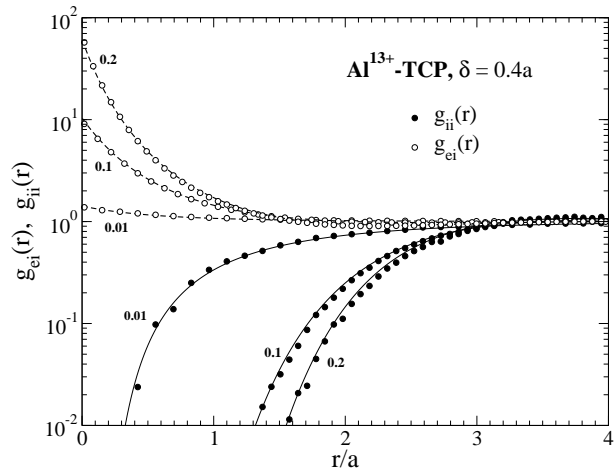


FIG. 5: Same as Fig. 4 for the RDFs  $g_{ei}(r)$  and  $g_{ii}(r)$  with  $\bar{\delta} = 0.4$ , and  $\Gamma_{ee} = 0.01, 0.1$ , and  $0.2$  as indicated by the numbers.

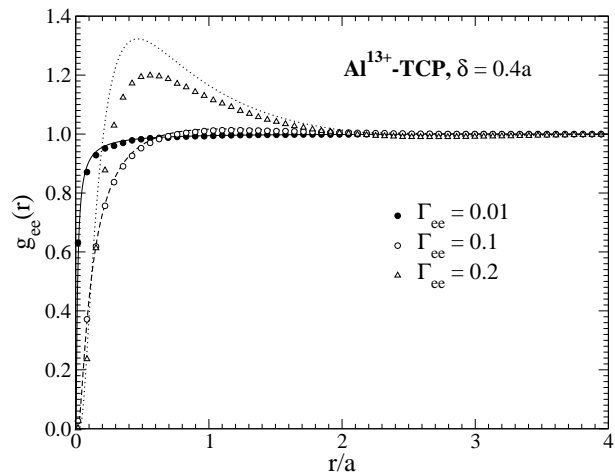


FIG. 6: Same as Fig. 5 for  $g_{ee}(r)$ .

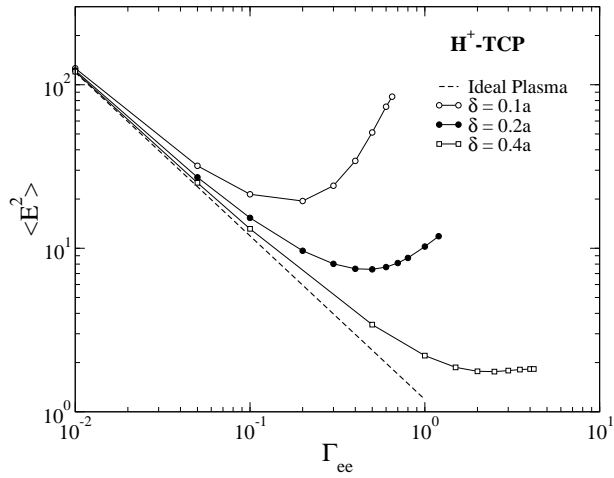


FIG. 7: The second moment  $\langle E^2 \rangle$  of the MFD (in units  $E_H^2$ , see Eq. (25)) obtained from the HNC scheme using Eq. (21) as a function of  $\Gamma_{ee}$  for a  $H^+$ -TCP. The dashed line corresponds to the limiting case of an ideal plasma (see the text for details). The lines with open and filled circles and squares represent the second moments for  $\bar{\delta} = 0.1$ ,  $\bar{\delta} = 0.2$  and  $\bar{\delta} = 0.4$ , respectively.

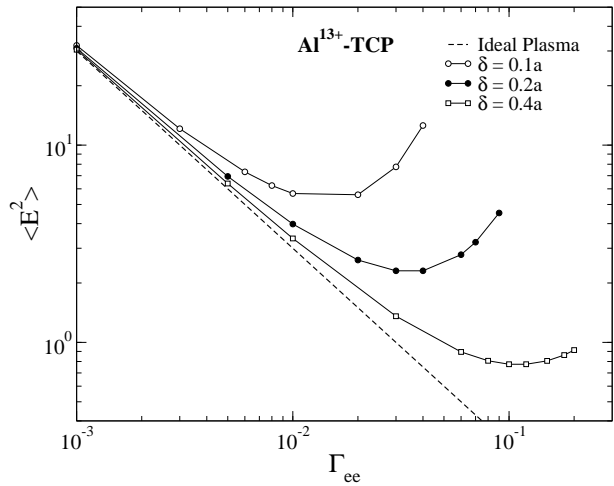


FIG. 8: Same as Fig. 7 for a  $Al^{13+}$ -TCP.

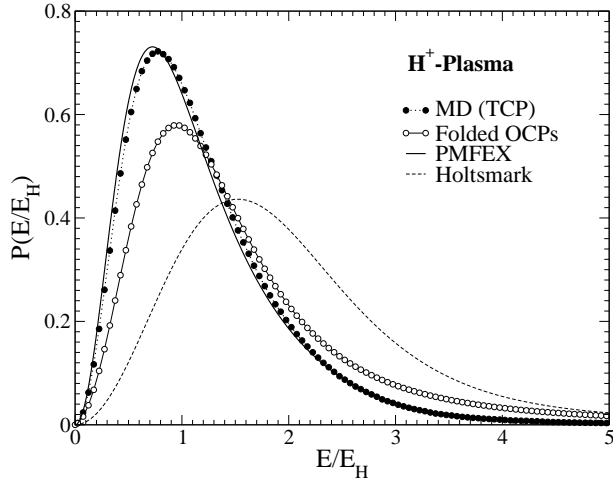


FIG. 9: Normalized electric microfield distributions for a hydrogen plasma with  $\Gamma_{ee} = \Gamma_{ii} = 1$  and  $\bar{\delta} = 0.4$  as a function of the electric field in units of  $E_H$ , Eq. (25). The filled circles represent the MFD from the MD simulations and the solid curve the results of the PMFEX. The open circles are the MFD obtained from the folding of an electronic and an ionic OCP, see Eq. (42). The Holtsmark distribution (see Eqs. (13) and (24)) is shown as a dashed line.

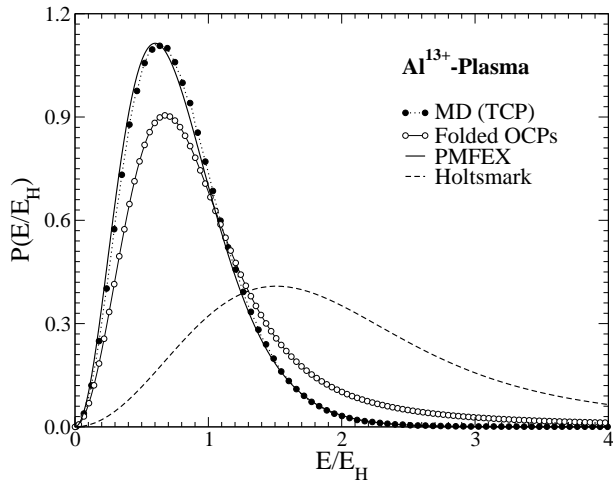


FIG. 10: Same as Fig. 9 for a  $\text{Al}^{13+}$  plasma with  $\Gamma_{ee} = 0.1$  and  $\Gamma_{ii} = 7.2$ .

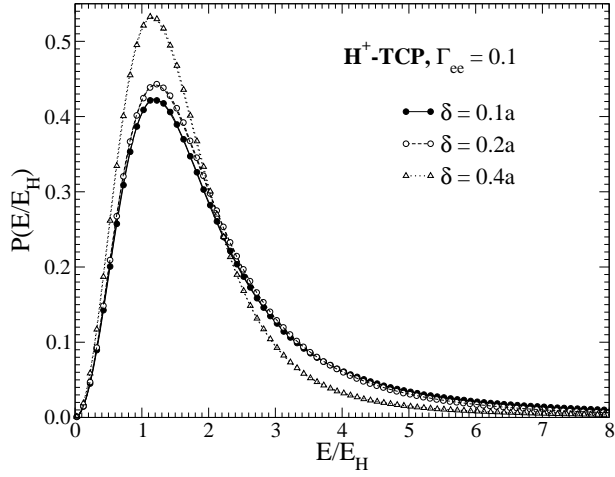


FIG. 11: Normalized electric microfield distributions for  $H^+$ -plasmas. The lines with and without symbols correspond to MD simulations and PMFEX approximation, respectively.  $\Gamma_{ee} = 0.1$  and  $\bar{\delta} = 0.1$  (solid lines), 0.2 (dashed lines), and 0.4 (dotted lines).

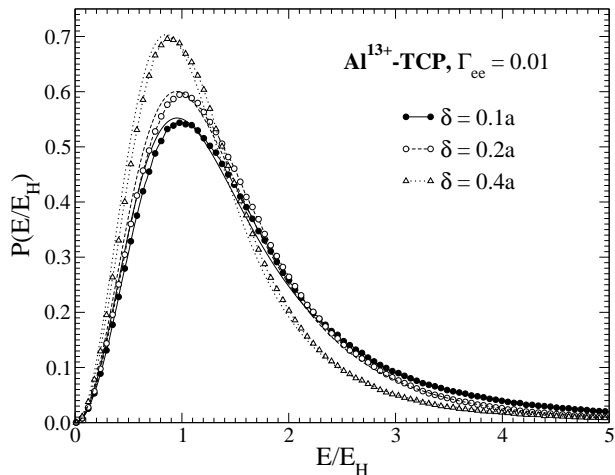


FIG. 12: Same as Fig. 11 for  $Al^{13+}$ -plasmas with  $\Gamma_{ee} = 0.01$ .

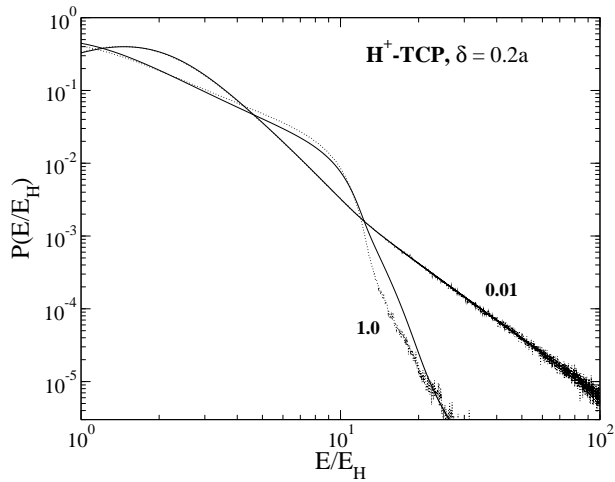


FIG. 13: MFDs in double-logarithmic plots for  $H^+$  plasmas with  $\bar{\delta} = 0.2$  and  $\Gamma_{ee} = 0.01$ ,  $\Gamma_{ee} = 1.0$  as indicated by the numbers. Here the solid curves represent the PMFEX approximation and the dotted curves MD simulations, respectively.

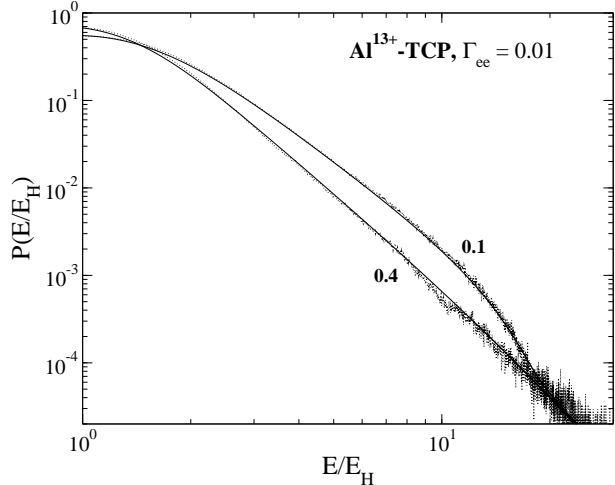


FIG. 14: Same as Fig. 13 for  $Al^{13+}$  plasmas with  $\Gamma_{ee} = 0.01$  and  $\bar{\delta} = 0.1$ ,  $\bar{\delta} = 0.4$  as indicated by the numbers.

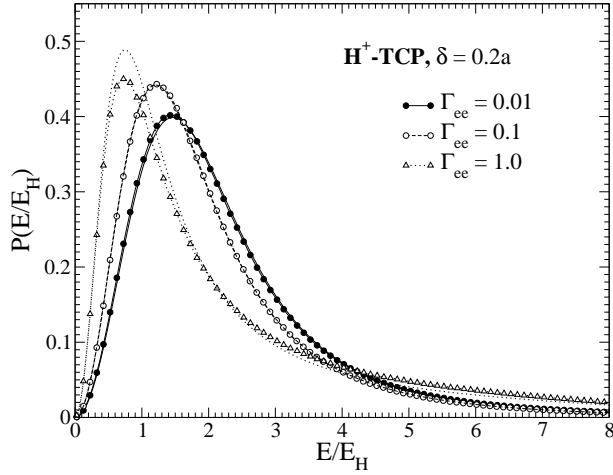


FIG. 15: Same as Fig. 11 with  $\bar{\delta} = 0.2$  and  $\Gamma_{ee} = 0.01$  (solid lines), 0.1 (dashed lines), and 1.0 (dotted lines).

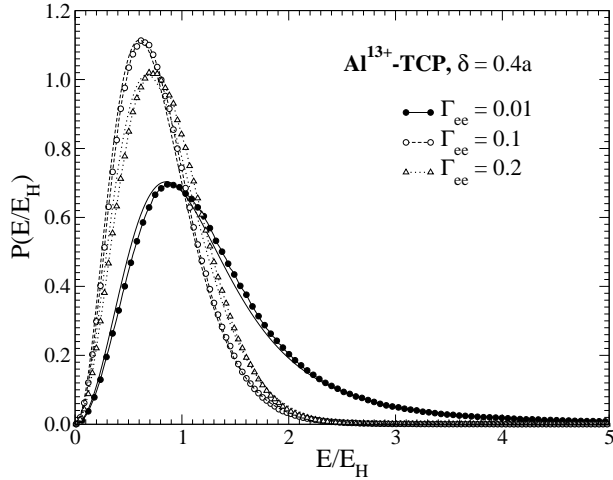


FIG. 16: Same as Fig. 12 with  $\bar{\delta} = 0.4$  and  $\Gamma_{ee} = 0.01$  (solid lines), 0.1 (dashed lines), and 0.2 (dotted lines).

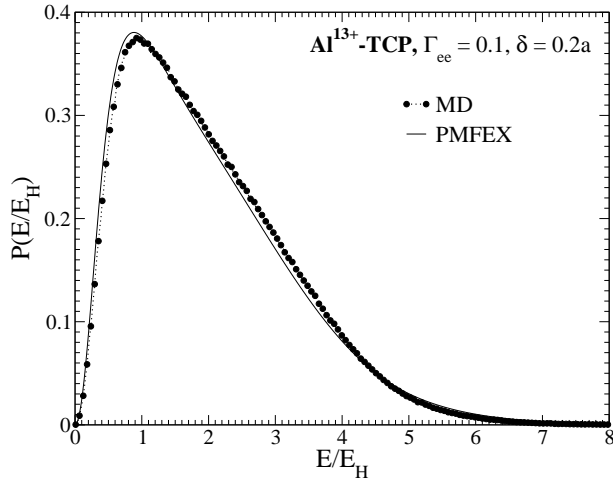


FIG. 17: Same as Fig. 12 for  $\bar{\delta} = 0.2$  and  $\Gamma_{ee} = 0.1$ .

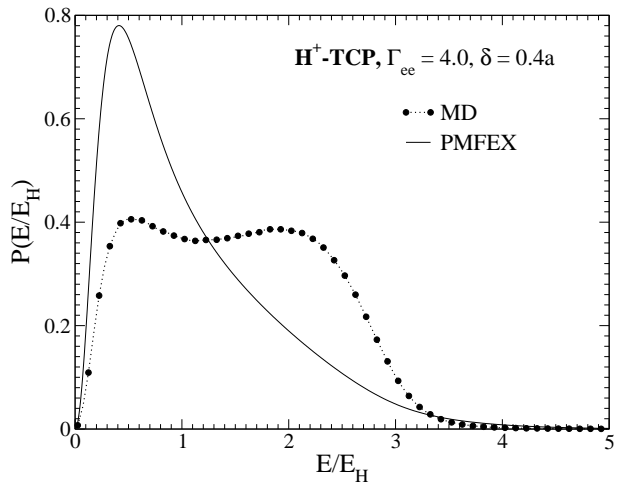


FIG. 18: Same as Fig. 11 for  $\Gamma_{ee} = 4.0$  and  $\bar{\delta} = 0.4$ .